Biophysical *Journal*
Article

Biophysical Society

Quantifying Fibrinogen-Dependent Aggregation of Red Blood Cells in Type 2 Diabetes Mellitus

Yixiang Deng,[1,2] Dimitrios P. Papageorgiou,[3] Xuejin Li,[4] Nikolaos Perakakis,[5] Christos S. Mantzoros,[5,6] Ming Dao,[3] and George Em Karniadakis[1,*]

[1]Division of Applied Mathematics and [2]School of Engineering, Brown University, Providence, Rhode Island; [3]Department of Materials Science and Engineering, Massachusetts Institute of Technology, Cambridge, Massachusetts; [4]Department of Engineering Mechanics and Center for X-Mechanics, Zhejiang University, Hangzhou, People's Republic of China; [5]Division of Endocrinology, Diabetes and Metabolism, Department of Internal Medicine, Beth Israel Deaconess Medical Center, Harvard Medical School, Boston, Massachusetts; and [6]Boston VA Healthcare System, Boston, Massachusetts

ABSTRACT Fibrinogen is regarded as the main glycoprotein in the aggregation of red blood cells (RBCs), a normally occurring phenomenon that has a major impact on blood rheology and hemodynamics, especially under pathological conditions, including type 2 diabetes mellitus (T2DM). In this study, we investigate the fibrinogen-dependent aggregation dynamics of T2DM RBCs through patient-specific predictive computational simulations that invoke key parameters derived from microfluidic experiments. We first calibrate our model parameters at the doublet (a rouleau consisting of two aggregated RBCs) level for healthy blood samples by matching the detaching force required to fully separate RBC doublets with measurements using atomic force microscopy and optical tweezers. Using results from companion microfluidic experiments that also provide in vitro quantitative information on cell-cell adhesive dynamics, we then quantify the rouleau dissociation dynamics at the doublet and multiplet (a rouleau consisting of three or more aggregated RBCs) levels for obese patients with or without T2DM. Specifically, we examine the rouleau breakup rate when it passes through microgates at doublet level and investigate the effect of rouleau alignment in altering its breakup pattern at multiplet level. This study seamlessly integrates in vitro experiments and simulations and consequently enhances our understanding of the complex cell-cell interaction, highlighting the importance of the aggregation and disaggregation dynamics of RBCs in patients at increased risk of microvascular complications.

SIGNIFICANCE Type 2 diabetes mellitus has long been a prevalent disease with complications such as diabetic retinopathy, kidney failure, and cardiovascular disease that reduce the life expectancy of patients. Here, we investigate the rouleau dissociation characteristics of diabetic red blood cells (D-RBCs) through patient-specific predictive simulations that are informed by companion microfluidic experiments. We identify the different rouleau breakup behaviors of D-RBCs and normal RBCs in a microfluidic device and quantify the fibrinogen-dependent aggregation strength of D-RBCs and normal RBCs. This study provides insights into the aggregation and disaggregation dynamics of rouleaux in patients with type 2 diabetes mellitus.

INTRODUCTION

Type 2 diabetes mellitus (T2DM) is characterized by relative insulin deficiency caused by pancreatic cell dysfunction and insulin resistance in target organs (1). Patients with T2DM usually suffer from elevated blood glucose and glycated hemoglobin (hemoglobin A1c, HbA1c) levels, which are important predictors of the risk of development for several microvascular complications, e.g., diabetic retinopathy (2,3) and diabetic peripheral nephropathy (4–6). Currently, it is understood that the impaired blood circulation of T2DM patients is a multifactorial event mainly due to endothelial dysfunction (7), platelet hyperreactivity (8–10), and red blood cell (RBC) hyperaggregatability (11,12). Under physiological condition, the linear stacking of RBCs forming a chain-like structure, called a rouleau, is a reversible process that occurs in low-speed blood flow (13). For metabolically healthy but obese patients, obesity is believed to be correlated with increased RBC aggregation (14–16). Under pathological condition like T2DM, RBC

Submitted March 23, 2020, and accepted for publication July 28, 2020.

*Correspondence: george_karniadakis@brown.edu

Yixiang Deng and Dimitrios P. Papageorgiou contributed equally to this work.

Editor: Mark Alber.

https://doi.org/10.1016/j.bpj.2020.07.026

hyperaggregatability leads to enhanced rouleau formation (17) in patient's blood, causing blood hyperviscosity in capillaries (18,19) and low oxygen levels in tissues (20).

The impaired blood circulation due to the enduring rouleau structures and altered RBC membrane property is undoubtedly a risk for the functionality of organs. Hence, understanding the blood cell dysfunction and quantifying fibrinogen-dependent RBC aggregation dynamics under normal or disturbed metabolism is of fundamental importance in diabetic research (21). It is recognized that both the concentration level of plasma fibrinogen and that of dextran are dominant factors in the formation of rouleaux. The fibrinogen molecule is considered to be the major plasma protein promoting RBC rouleau formation (22), and the synthetic polymer dextran can also promote the formation of RBC aggregates (23–26). Several studies have been conducted to explore the RBC-RBC aggregation strength using different in vitro flow experiments (27,28). For example, Chien et al. performed experiments in a flow channel to find that a 50% separation of a 2-cell rouleau (doublet) suspended in dextran solution occurs at a critical shear stress of 0.25 ± 0.01 dyn/cm^2 (23). Samocha-Bonet et al. visualized the aggregation process of RBCs suspended in autologous plasma or dextran-500 kPa for obese and nonobese patients, respectively, under controllable shear stress in a flow chamber (29). They showed that plasma of obese patients is a powerful stimulator for RBC aggregation, producing large clusters of aggregates that were resistant to dispersion by flow, and concluded that among the plasma components, fibrinogen is a well-characterized RBC aggregation inducer that bridges between RBCs. Several groups have also utilized optical tweezers (OT) to study the RBC aggregation and disaggregation dynamics in plasma and protein solutions (30–32). They found that the critical detachment force required to fully separate the RBC doublets ranges from 10 to 20 pN (31). In addition, Avsievich et al. (33) employed OT to investigate the dynamics of rouleau formation in dextran and fibrinogen solutions. They found that these two polymers present distinct aggregation mechanisms in the RBC aggregation dynamics (33). Atomic force microscopy (AFM) has also been used to investigate the aggregation properties of RBCs. For example, Steffen et al. applied AFM to determine the effect of dextran concentration on the interaction energy of RBC doublets (34). They measured the interaction forces varied from 14 to 23 pN for dextran 70 and from 43 to 169 pN for dextran 150. Guedes et al. (35,36) conducted AFM-based experiments on RBC doublets for patients with essential arterial hypertension in plasma solution. They found that the critical force required to fully break up the RBC doublets from an essential arterial hypertension patient's blood is ~180 pN, which is about twice as much as those of the healthy RBC doublets (35,36).

Along with the experimental studies, recent advances in computational modeling and simulations have also contributed to the understanding of the aggregation dynamics of RBCs under physiological and pathological conditions (13,25,37–42). For example, Xiao et al. employed dissipative particle dynamics (DPD) to simulate the deformation and aggregation of healthy RBC doublets (37) and their effects on the blood flow dynamics in stenosed microvessels (38). They found that the blood flow resistance decreases with the increased intercellular interactions when the RBC doublets passed through the stenosis. Flormann et al. (25) carried out numerical simulations and developed theoretical models to characterize the interaction energy of RBC doublets. They found that the RBC doublet deformation increases nonlinearly with the interaction energy (25). Some researchers also investigated the dynamics of rouleau formation under diseased states. For example, Ye et al. showed that malaria-infected RBC doublets become harder to separate with the increase of capillary number (39). They also showed that both the cell deformation and cell-cell aggregation interaction can affect the trajectory of RBC doublets in microvascular bifurcations (40). Fedosov et al. employed a multiscale RBC (MS-RBC) model to investigate the effect of cell-cell aggregation interaction on blood viscosity at different shear rate (13). They identified that the types and sizes of RBC rouleau structures can yield a significant increase of blood viscosity at low shear rates. They also systematically studied the shapes of RBC doublets under different adhesion strength and shear elasticity (43). They found that the adhesion strength and membrane properties play key roles in determining the doublet phases.

Despite these aforementioned findings, many important aspects of aggregation dynamics of diseased RBCs are still poorly understood. It is known that the RBC deformability and aggregation properties are altered in T2DM blood, but individual patients with T2DM have a highly variable clinical phenotype. For this reason, there is a compelling need to develop a predictive patient-specific RBC model to quantify the aggregation and disaggregation dynamics of RBCs in T2DM. Such a model would provide a more reliable method and an overall modeling framework to extract aggregation properties of T2DM RBCs from a variety of independent experimental methods. In this work, we aim to first establish patient-specific RBC models that invoke key parameters derived from microfluidic experiments and subsequently to investigate the fibrinogen-dependent aggregation dynamics of T2DM RBCs through patient-specific computational simulations. To build such multiscale patient-specific models, we develop a workflow that incorporates useful experimental data and utilizes simulations as a surrogate tool for quantitative investigations of cell mechanical and rheological properties, although some critical parameters cannot be provided directly by microfluidics, AFM, or OT experiments (i.e., these physical parameters can only be inferred through a simulation model closely following the experimental setup). The motivation for this work is to demonstrate that by incorporating the data from

experiments and simulations, our predictive computational model could be employed to quantify patient-specific and fibrinogen-dependent RBC aggregation dynamics. Specifically, we quantify the fibrinogen-dependent aggregation of RBCs from six patients with disparate severity of metabolic syndromes and T2DM (i.e., three patients with T2DM and the other three patients without T2DM, marked by distinct plasma fibrinogen concentrations; see Table 1) through patient-specific predictive computational simulations that invoke key parameters derived from in vitro microfluidic experiments. We note that these six patients are obese, indicated by their body mass indices and metabolic parameters in Table S1. In the microfluidic experiments, we employed a microfluidic device consisting of an ordered array of microgates that mimic the structure and characteristics of microvascular capillaries (44–46). In the numerical simulations, we combined previously validated MS-RBC model for RBCs in T2DM patients (47,48) and in obese patients with cell-cell aggregation model to capture the functional dependence of doublet breakup force on fibrinogen concentration in (31,35).

Motivated by the phenomenon that patients exhibit heterogeneous distribution of rouleau length (rouleau length denotes the number of RBCs in the rouleau; see Fig. 1), we hypothesize that every patient's blood sample may have different levels of RBC aggregation strength, whose distribution can be inferred from the rouleau length distribution observed under controlled flow condition. Based on this hypothesis, we first quantify the cell-cell adhesion strength through matching the experimental measured detachment forces required to separate RBC doublets under different fibrinogen concentration (31,35). Then, informed by our companion in vitro microfluidic experiments, we perform numerical simulations to study the traversal of patient-specific RBC doublets through microgates. We compare the simulated RBC doublet dissociation rate (the number of RBC doublets broken apart over the total number of RBC doublets observed in the region of interest (ROI)) with those obtained in microfluidic experiments. Next, using the calibrated parameters, we present some additional simulations to probe the cell-cell detachment dynamics of the RBC rouleaux with chain-like structures under different inclination angles to the overall flow direction.

METHODS

Experimental data

Subject recruitment, blood sample preparation, and biochemical measurements

All studies involving human blood were approved by the institutional review board of the Beth Israel Deaconess Medical Center and the Massachusetts Institute of Technology. Blood samples from six obese patients were collected for this study at Beth Israel Deaconess Medical Center. Patients were selected with different chronic glucose conditions, i.e., three without T2DM and HbA1c $< 6\%$ (subject I–III) and three diagnosed with T2DM and HbA1c $\geq 6\%$ (subjects IV–VI). Plasma fibrinogen concentration level for each patient was measured with an enzyme-linked immunosorbent assay (Abcam, Burlingame, CA). In general, patients with T2DM have high levels of plasma fibrinogen compared with those without T2DM, which is consistent with the observations in (49). A detailed lab report is shown in Table 1, and see Table S1 for patients' metabolism measurements, including medications.

All blood samples were collected into separate 4 mL K2-EDTA spray-coated anticoagulant vacutainers (7.2 mg/4 mL). Deidentified samples were transferred to the Massachusetts Institute of Technology within 3 h of blood draw and were processed immediately. After whole blood density gradient centrifugation at 820 relative centrifugal force (or $\times$ g, where g stands for gravitational force) for 5 min, the blood plasma was removed and kept in a separate tube; also, the buffy coat was removed and discarded. To remove the anticoagulant, packed RBCs were washed twice for 5 min under centrifugation. The RBCs were then resuspended in autologous plasma, giving a hematocrit at 2–3%. Low-retention pipette tips were used throughout blood processing.

Microfluidic experiments

To study the rouleau dynamics under flow, we conducted experiments within microfluidic devices; see Fig. 2 *A*. In brief, the devices comprise a free-standing gas-permeable polydimethylsiloxane (PDMS) membrane ($H_{\mathrm{PDMS}} = 150$ μm) within a dual-layer microchannel construction. The dual-layer device consists of a "flow microchannel" in which there is flow of RBC suspension and a "gas microchannel" in a cross configuration. In this work, we only utilized the flow microchannel, which is 3 mm in

TABLE 1 Complete Blood Count Analysis and the Enzyme-Linked Immunosorbent Assay Test Results

Patient ID	I	II	III	IV	V	VI
Information	Obese	Obese	Obese, HBP, HLD	Obese, T2DM	Obese, T2DM, HBP	Obese, T2DM, HBP, HLD
HbA1c, %	5.8	5.3	5.5	6.2	8.6	6.9
Fibrinogen, mg/mL	4.656	2.641	3.114	3.373	5.122	3.985
Hb, g/dL	15.2	17.8	14.1	11.9	14.5	12.7
HCT, %	44.6	50.3	39.8	39.3	43.5	39.1
RBC, $\times 10^6$ count/μL	4.97	5.52	4.38	5.72	4.96	4.51
WBC, $\times 10^3$ count/μL	8.8	5.4	4.9	6.7	6.1	4.7
MCV, fL	90	91	91	69	88	87
MCH, pg	30.6	32.3	20.8	29.2	29.2	28.2
MCHC, g/dL	34.1	35.4	35.4	30.3	33.3	32.5
RDW, %	13.5	13.0	13.4	17.0	13.5	14.2

Abbreviations: HBP, hypertension; HLD, hyperlipidemia; HbA1c, glycated hemoglobin; Hb, total hemoglobin; HCT, hematocrit; RBC, red blood cell count; WBC, white blood cell count; MCV, mean corpuscular volume; MCH, mean corpuscular hemoglobin; MCHC, mean corpuscular hemoglobin concentration; RDW, red cell distribution width.

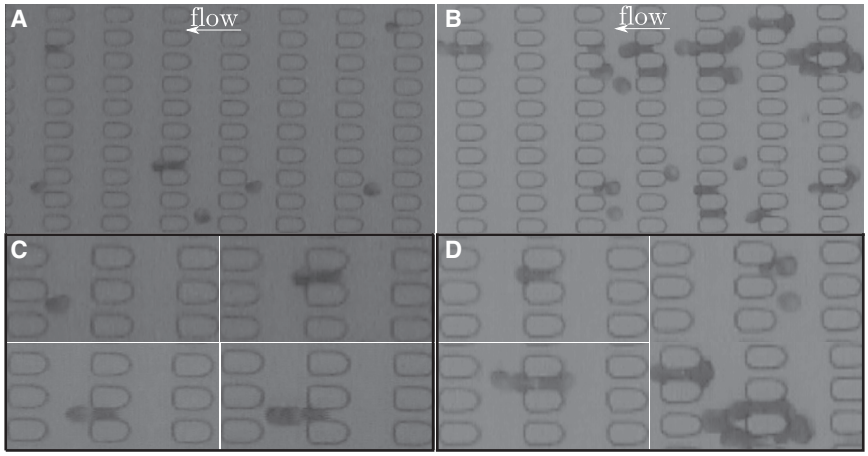

FIGURE 1 Rouleau structures inside the microfluidic device for (*A*) patient II (no T2DM) and (*B*) patient V (poorly controlled T2DM). Zoomed-in rouleau structures of different lengths are shown (*C*) for patient II, which are a singlet (*upper left*), a doublet (*upper right* and *lower left*), and a triplet (*lower right*), and (*D*) for patient V, which are a singlet (*upper left*), a doublet with a singlet (*upper right*), and several multiplets (*lower left* and *lower right*). See Video S1 for patient II and Video S2 for patient V and see Table 1 for patients' information.

length and 1.326 mm in width and is connected to in-line pressure and flow sensors. The flow microchannel consists of periodic obstacles with 15-μm-long, 4-μm-wide, and 5-μm-high microgates (marked in Fig. 2 *A*), mimicking the mechanical challenges RBCs encounter when passing through the smallest capillaries or spleen slits in the human body (44,46). Before being filled with the RBC-plasma suspension, the microfluidic device was degassed for a minimum of 10 min to prevent trapping of air bubbles.

Microfluidic device imaging was performed using Zeiss Axiovert 200 (Zeiss, Oberkochen, Germany) and Olympus IX71 inverted microscopes (Olympus, Tokyo, Japan). A Hitachi KP-D20A (Hitachi, Tokyo, Japan) charge-coupled device and Olympus DP72 cameras (Olympus, Tokyo, Japan) were used for image acquisition. All testing was performed at 37°C using the ibidi heating system (ibidi USA, Fitchburg, WI) as a heating incubator.

Simulation models and methods

RBC models

To investigate the mechanical, rheological, and dynamic properties of RBCs at different length scales, we have developed a unified multiscale modeling framework based on DPD (50–52). Specifically, the membrane of RBC was modeled by a two-dimensional triangulated network with N_v vertices connected by N_s edges and N_t triangles. With the help of the MS-RBC models, we have conducted a variety of simulations to probe a broad range of mechanical and rheological problems associated with RBCs under normal and pathological conditions, including T2DM (13,45,53–56). Following our prior simulations on T2DM RBCs (47,48), we performed simulations with two types of MS-RBC models: one characterized the morphological and mechanical properties of normal RBCs (N-RBCs), and the other mimicked those of T2DM RBCs (D-RBCs) (Fig. 2 *B*). Both the N-RBC and the D-RBC maintained similar cell surface area $A_0^N = A_0^D = 132.9\ \mu\text{m}^2$ but had different morphological characteristics; the N-RBC in a static condition was characterized by a biconcave shape with cell volume $V_0^N = 92.5\ \mu\text{m}^3$, whereas the D-RBC was characterized by a more oblate shape with cell volume $V_0^D = 127.4\ \mu\text{m}^3$. Specifically, the N-RBC was modeled with shear modulus $\mu_0^N = 4.73\ \mu$N/m and bending rigidity $k_0^N = 2.4 \times 10^{-19}$ J and the D-RBC with shear modulus $\mu_0^D = 2\mu_0^N$, considering the decreased RBC deformability in diabetics (11,57) and bending rigidity $k_0^D = k_0^N$. Detailed formulas for pairwise interaction potentials to maintain the morphology and mechanical property of RBCs can be found in the Supporting Materials and Methods. In this study, we extended these two MS-RBC models and investigated the (dis)aggregation dynamics of T2DM RBCs. In most simulations, we have used $N_v = 500$, a coarse-grained RBC model that has been employed to conduct efficient simulations of RBCs in microcirculation. For comparison, we also considered a much finer MS-RBC model with $N_v = 2000$. An example of simulation snapshot in this study is shown in Fig. 2 *C*.

Cell-cell interaction models

The aggregation interaction between RBCs plays a major role in determining the size and shape of the RBC aggregates. As suggested by Fedosov et al. (13), we employed the Morse potential to model fibrinogen-dependent intercellular aggregation interactions. The Morse potential reads

$$U_M(r) = D_0\left[e^{2\beta(r_0-r)} - 2e^{\beta(r_0-r)}\right], \tag{1}$$

where D_0 denotes the depth of the potential well, e is the base of the natural logarithm, r denotes the distance between two vertices, r_0 represents zero force distance, and β represents a distance scaling constant. Specifically, the Morse potential is imposed on a specific type of vertices, called "interactive vertices," represented by the blue vertices in Fig. 2 *D*. In addition, we imposed the repulsive term of the Lennard-Jones potential on the membrane vertices to prevent the RBC membranes from overlapping. The corresponding potential is given by

$$U_{LJ}(r) = 4\epsilon\left[\left(\frac{\sigma}{r}\right)^{12} - \left(\frac{\sigma}{r}\right)^{6}\right], \qquad (r \le r_{\text{LJ}}), \tag{2}$$

where r_{LJ} is the cutoff distance and ϵ and σ are scaling constants for energy and distance, respectively. Detailed model parameters can be found in the Supporting Materials and Methods.

Fibrinogen-concentration-dependent RBC models

To construct RBC models that reflect the different levels of cell-cell adhesion strength, we adopted the hypothesis that rouleau formation is mainly due to the "cross-bridging" effect created by the binding of each end of a fibrinogen molecule to two different RBCs (58). In the "cross-bridging" hypothesis, the pairwise connection (the bridges) strength between "interactive vertices" is considered to be a fixed value, and hence, more established bridges between two different cells will lead to stronger adhesion between cells. The adhesion strength of each bridge is mainly correlated with the parameter D_0 in Eq. 1. in our cell-cell interaction model. In addition, Lominadze and Dean (71) showed the existence of fibrinogen-specific binding to the RBC membrane surface, and their results implied that the number of total bindings is positively correlated with the concentrations

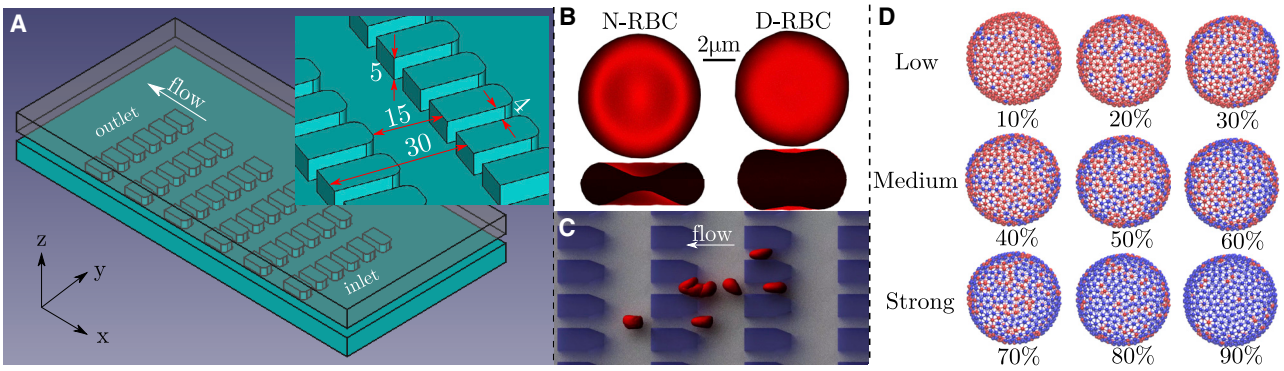

FIGURE 2 Overview of the simulation setup. (*A*) A schematic representation of the microfluidic device with periodic obstructions. Schematics are not drawn to scale, and the dimensions are in microns. (*B*) Schematics of a normal (healthy) RBC (N-RBC) and a T2DM RBC (D-RBC) models. An N-RBC in equilibrium maintains a biconcave shape with surface to volume ratio, $S/V = 1.44$, whereas a D-RBC maintains a more oblate shape with $S/V = 1.04$. (*C*) A simulation snapshot of T2DM rouleau breakup when passing through microgates under flow. (*D*) The cell-cell interaction model, which simulates the fibrinogen-concentration-dependent cell-cell interaction strength. Blue vertices denote "interactive vertices" (IVs) responsible for attractive interactions with vertices of the same type on other RBCs, whereas red vertices do not exhibit attractive interactions. Numbers below each cell represent the ratio (in percentage scale) of the number of IVs/the total number of vertices on the membrane. Based on the ratio, models are divided into three groups, i.e., low, medium, and strong groups, simulating cell-cell adhesive interactions with low, medium, and strong aggregation strength, respectively, and implicitly address low, medium, and high fibrinogen concentration level, respectively. To see this figure in color, go online.

of human plasma fibrinogen within a certain range of fibrinogen concentration level. Herein, we varied the percentage of the "interactive vertices" corresponding to equivalent different fibrinogen concentration levels to describe the different levels of rouleau adhesion strength, i.e., low, medium, and high level (see Fig. 2 *D*). These RBC models were later modified to characterize patient-specific RBCs in simulations. We note that the geometry and arrangement of the microgates in the simulations followed those in companion experiments, as shown in Fig. 2 *A*. The dimensions of the simulation domain are 180 μm in length, 60 μm in width, and 12 μm in length. Periodic boundary conditions were applied in the x and y directions, and the flow was bounded by solid walls in the z direction. In all simulations, the solid walls were modeled by freezing layers of particles with bounce-back reflection to satisfy the no-slip boundary condition (59). An external body force was exerted on all fluid particles and RBCs along the x direction to generate a flow in the microchannel.

RESULTS AND DISCUSSION

In this study, we aim to establish patient-specific RBC models and simulate the dynamics of patient-specific rouleaux at the doublet and multiplet levels. Specifically, we seamlessly integrate experimental data from both existing literature and our own microfluidic experiments following the flow chart shown in Fig. 3. At the "Input" stage, we first quantify the parameters in our cell-cell adhesive interaction model—most importantly, the coefficient D_0 in the Morse potential—through benchmark simulations mimicking AFM and OT experiments by other researchers. Second, we construct the flow field in our simulations such that the single RBC velocity in simulations matches that in our experiments; consequently, we obtain the relationship between driving pressure gradient and cell velocity. Third, we analyze the dynamics of rouleaux in our microfluidic experiments from different patients' blood samples and build patient-specific RBC models accordingly. At the "Inference" stage, we incorporate the "Model" parameters for simulations of rouleau dynamics inside the microfluidic device. First, we validate the patient-specific cell-cell interaction models at doublet level by comparing the doublet dissociation rate obtained from experiments and simulations. Second, at the multiplet level, we compare the breakup patterns of two 10-cell rouleaux, in which these two rouleaux travel through microgates with two different angles between the rouleau centerline and the flow direction.

Quantification of fibrinogen-dependent cell-cell adhesion strength at doublet level

In analogy with the experimental setups (31,35), we perform simulations in which initially one RBC is placed on top of another RBC to form a doublet, as shown in Fig. 4, and then the top RBC is pulled away from the bottom RBC. The RBC-wall adhesion is simulated by keeping stationary the lower half vertices on the bottom RBC membrane. In the simulation, cell-cell adhesion between the two stacked RBCs occurs spontaneously after they approach each other (here, "spontaneously" refers to the condition that no extra force is exerted on the top RBC to induce cell-cell adhesion, i.e., the top RBC is not pressed to the bottom RBC to form contact but is carefully laid on the bottom one). After sufficient contact time and the cell-cell interaction reaching an equilibrium, we impose a stepwise increasing pulling force on the top RBC until the doublet breaks up, i.e., these two RBCs are fully detached from each other. The number of pulling vertices is ϵN_v, where ϵ is the vertex fraction. In the AFM experiment, the AFM tip is positioned above the RBC center, which generates a breakup pulling force on the vertical direction normal to the RBC discoid surface,

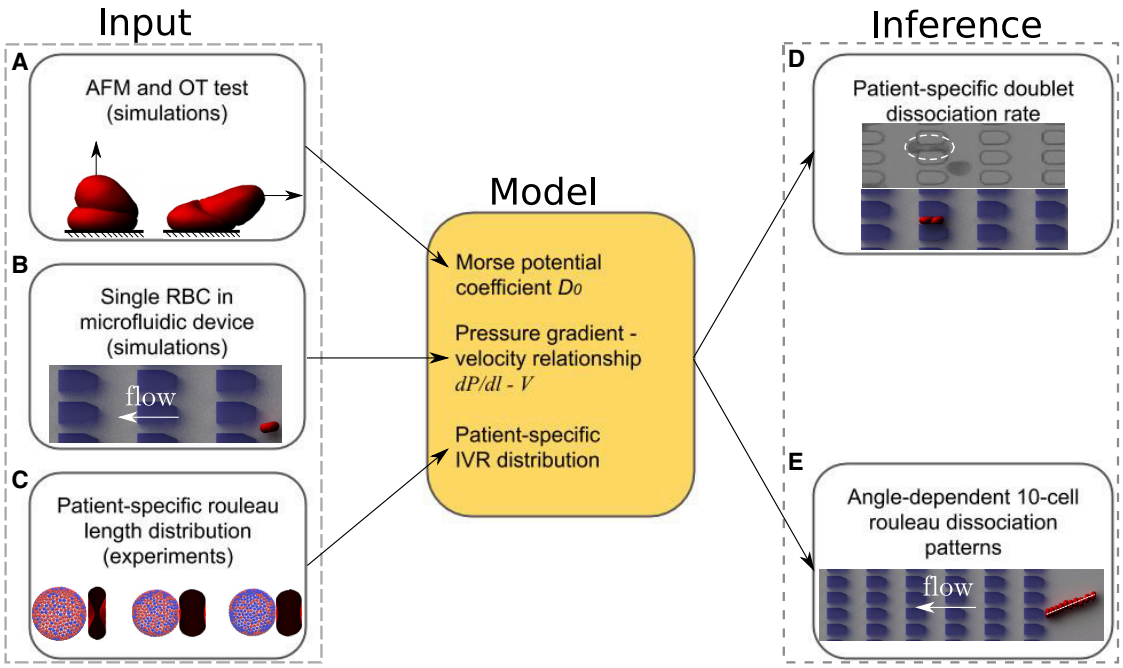

FIGURE 3 Flow chart of simulation setup for hypothesis validation. (*A*) Existing AFM and OT experiments were used to calibrate the parameters of the cell-cell interaction models. Based on the detaching forces, Morse potential coefficient D_0 were obtained. (*B*) Single-cell simulations of N-RBCs and D-RBCs were performed, passing through microgates under varying pressure-gradient values. The dependence of the single-cell velocity, *V*, on the pressure gradient, *dP*/*dl*, of N-RBCs and D-RBCs, respectively, was obtained. (*C*) In-house microfluidic experiments were performed under comparable flow conditions. Higher levels of fibrinogen concentration from patient samples possessed long rouleau chains more frequently. We measured the distribution of singlets, doublets, and multiplets by taking snapshots of the rouleau within the ROI. These distributions guided the simulation scheme of the interactive vertices ratio (IVR, γ). (*D*) Probing the rouleau breakup dynamics under different fibrinogen concentration levels by comparing patient-specific doublet dissociation rates observed in experiments with that obtained from simulation. (*E*) Angle-dependent 10-cell rouleau dissociation simulations to highlight the predictive capability of our model for complex flow behaviors involving aggregatable cells. To see this figure in color, go online.

leading to a uniform cell-cell separation or a peeling breakup. In the OT experiment, the optical trap is positioned on the side of the RBC, which generates a breakup force along the horizontal direction parallel to the RBC discoid surface; hence, the two aggregated RBCs are pulled apart by sliding. Taking all these facts into consideration, we used a higher ϵ-value for matching simulation with the AFM test compared with that for the matching simulation with the OT test; i.e., we chose $\epsilon \approx 0.36$ for AFM (see Video S3) and $\epsilon \approx 0.2$ for the OT test (see Video S4).

In addition to the simulations on the cell-cell detachment of healthy doublets under different fibrinogen concentration levels, we also carry out the simulations on the breakup of T2DM doublets (see Fig. 5) and record an estimation of the critical forces, i.e., the minimal force that allows the full separation of these two cells in doublets. Generally, the cell-cell detaching force increases as the interactive vertices ratio (fibrinogen concentration level) increases in both AFM and OT experiments and simulations. Also, larger D_0 introduces the condition that a higher force is required to break up the doublets, i.e., the cases with $D_0 = 4.24 \times 10^{-25}$ J require higher detaching forces compared with those with $D_0 = 8.48 \times 10^{-26}$ J.

For the simulations mimicking OT (see Fig. 5 *A*), the critical force *F* of healthy doublets (*black dashed line*) saturates to a mean value around 10 pN, whereas the critical force of T2DM doublets does not saturate smoothly to a plateau value but has a further increase at high interactive vertices ratio γ. A typical simulation video clip on the cell-cell detachment of T2DM doublet with OT test is provided in Video S5. As shown in the video, when the top RBC of a T2DM doublet is pulled horizontally, the oblate shape of D-RBC induces a rotational motion of the top RBC around the bottom one, promotes the formation of additional binding sites during the detachment process, and hence reinforces adhesion between these two aggregated RBCs. As a result, the critical force *F* in T2DM doublets is higher than that in the healthy ones. Under the AFM test in Fig. 5 *B*, we found that the critical force *F* increases with the interactive vertex ratio γ (which is positively correlated with the fibrinogen concentration level) at low γ, whereas it smoothly approaches saturation at high γ. However, there appears to be a gap in the critical force obtained from computation and experiment. The discrepancy could arise from the the process and analysis of experimental data in (35). In their experiment, the maximal detachment force is ~70 pN even in the absence of fibrinogen, which is probably due to the presence of residual fibrinogen molecules coming from the plasma. If we treat it as the baseline value and perform a correction on the experimental data, we found that our

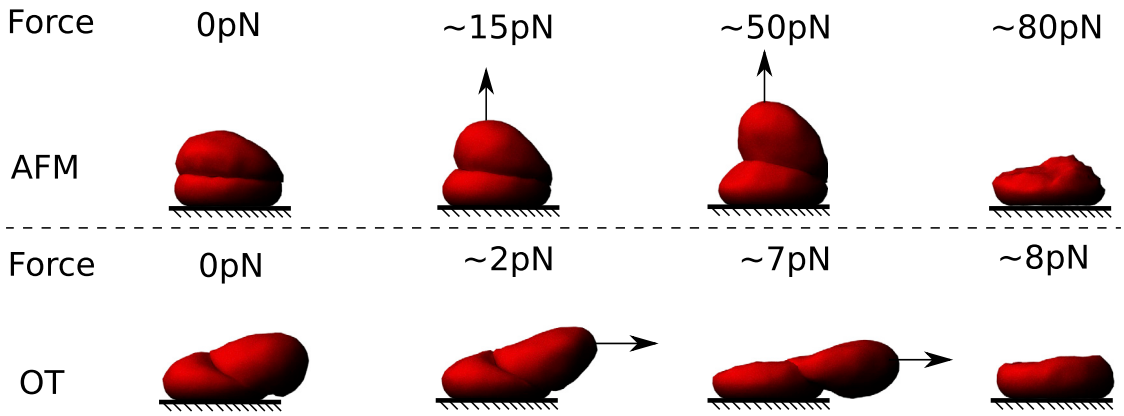

FIGURE 4 Schematic depiction of the simulation in which stepwise increasing force is exerted on the top RBC of a healthy doublet with AFM (*top row*) and OT test (*bottom row*). RBCs with full coverage of IVs are used, and the value on top of the doublets represents the force magnitude at each instant. In the last columns (*last snapshots*), the doublets break up; hence, only one RBC is shown. Video clips can be found in Video S3 for AFM test and Video S4 for OT test. To see this figure in color, go online.

predicted data fall into the range of the experimentally measured data. In addition, at the same D_0, we found that the critical forces necessary to detach two aggregated N-RBCs are higher than those for two aggregated D-RBCs. It probably arises from the oblate shape of D-RBC, which causes fewer interactive vertices, leading to fewer possible bindings on the contact surface between two RBCs. A video clip for a typical simulation on the breakup of T2DM doublet with AFM test is provided in Video S6. For comparison, we also simulated the RBC suspension and studied the cell-cell detachment at a much finer MS-RBC model with $N_v = 2000$; see Fig. 5 *B*. In analogy to a previous computational study by Hoore et al. (43), the adhesion strength Γ is directly proportional to the vertex density N_v/A_0^D, i.e., $\Gamma \sim D_0 N_v/A_0^D$; hence, the value of D_0 has dropped four times for the DPD case with $N_v = 2000$. We found that the critical force F-value decreases somewhat with finer DPD resolution. For example, for $\gamma = 0.5$, the value of critical force drops slightly from 47.6 pN with $N_v = 500$ down to 44.9 pN with $N_v = 2000$. However, because the deviation is sufficiently small, the coarse-graining level on the cell-cell aggregation does not affect our results.

Mesoscopic simulation of patient-specific single RBC dynamics

We employ a specially designed microfluidic device as shown in Fig. 2 *A* to study patient-specific cell-cell detachment dynamics of rouleaux. In the following, we present the

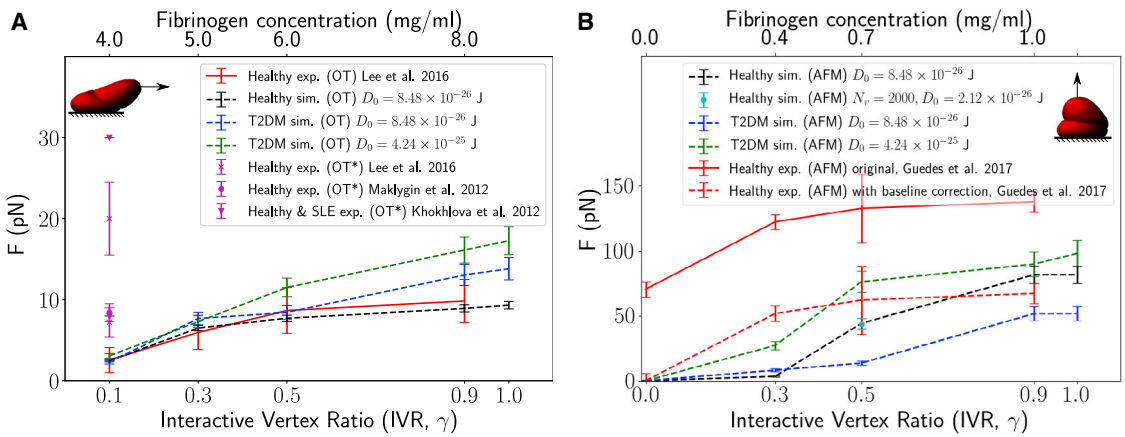

FIGURE 5 Quantitative validation of doublet breakup forces F with simulations mimicking OT and AFM on healthy and T2DM doublets. The top horizontal axes denote fibrinogen concentration level in experiments, and the bottom horizontal axes denote the IVR of the RBC models in simulation; exp. is short for experiment and sim. for simulation. (*A*) The result of the simulation mimicking the OT test with N-RBC doublets fits well with data from Lee et al. (31); hence, the corresponding Morse potential coefficient $D_0 = 8.48 \times 10^{-26}$ J is applied in later simulations mimicking microfluidic experiments. Note that when IVR exceeds 0.5, T2DM doublets require a larger detaching force than healthy doublet because of the oblate shape of the D-RBC. (*B*) The result of the simulation mimicking the AFM test with an N-RBC, which is quantitatively comparable with the experimental data with a baseline correction (all experimental data subtract the first experimental point at zero fibrinogen concentration) from Guedes et al. (35). The simulations were conducted using the MS-RBC model with $N_v = 500$, except for one simulation case at $\gamma = 0.5$ (*green solid circle*), in which we consider a finer MS-RBC model with $N_v = 2000$. Note that data points with * in the legend denote unclear fibrinogen concentration level. To see this figure in color, go online.

results of the blood samples from patients II, IV, and V listed in Table 1 because they represent three different common clinical conditions of increasing severity, i.e., obesity without T2DM and obesity with good and obesity with poor control of T2DM, respectively, indicated by the HbA1c level. Here, we focus on reproducing the dynamics of a rouleau in an ROI, i.e., a zoomed-in domain in which rouleau breakup occurs and from which we can infer the local fluid dynamics.

From the video clips of our microfluidic experiments, we record the time-dependent locations of single RBCs that are close to the rouleau of interest. On the other hand, we simulate the dynamics of single N-RBCs and D-RBCs passing through microgates in a range of pressure gradients (see Fig. 6). The simulation results show that under a fixed pressure gradient, the trajectory of both the single N-RBC and the D-RBC maintains a periodic pattern because of the periodicity of obstacles. We fit the trajectories of the RBCs to estimate their velocities under different pressure-gradient values for N-RBC in Fig. 6 *B* and for D-RBC in Fig. 6 *C*; see also Fig. 6 *D* for the fitted single RBC velocities under different pressure-gradient values. We find that the cell velocity is generally proportional to the pressure gradient within the simulated pressure-gradient range. In addition, we find that there is a minimal pressure gradient to start the motion of RBCs inside the microchannel to overcome the resistance due to the obstacles. We also compare the simulation results against available experimental data from Bow et al. (60), in which they studied the dynamics of malaria-infected RBCs inside a microfluidic device similar to ours. The shear modulus of malaria-infected RBCs is much greater than N-RBCs (61,62), which prohibits a malaria-infected RBC from traveling as fast as an N-RBC under the same pressure gradient. Although not as stiff, D-RBCs also travel more slowly compared with N-RBCs (11,63,64).

Next, we monitor the trajectories of three single RBCs in the blood sample of each patient and use linear fitting to obtain the corresponding mean velocities (see Fig. 7, *B*–*D*). As shown in the figures, the velocities of three RBCs do not vary dramatically for a certain patient. Hence, we can calculate the mean velocity from these three sampled velocities and take it as equal to the mean flow velocity in this small ROI. To quantify the pressure gradient required for patient-specific simulations, we use interpolation to obtain the pressure gradient required from Fig. 6, *B* and *C* and validate the single-RBC dynamics under the assumed pressure gradient; see Fig. 7 *B* for validation with an N-RBC and Fig. 7 *D* for validation with a D-RBC.

Patient-specific cell-cell detachment in microfluidic device at the doublet and multiplet levels

To perform experiment-informed patient-specific simulations, we construct patient-specific cell-cell interaction models by learning the intrinsic relationship between the interaction model parameters and in vitro rouleau length distribution. In the following, our targeted patients are patient II, IV, and V, as in the previous section. From the experiment, we observe the microfluidic experiment videos for each patient and gather two types of statistics. First, we randomly choose 10 frames of time-independent snapshots from each patient and count the number of singlets (a single RBC; we include singlet as a rouleau because it is meaningful as the most basic cell-cell adhesion element), doublets, and multiplets within the ROI. Then, we calculate the percentage of each type of rouleau for each patient (see Fig. 8 *B*). Note that the sum of these three percentages is 100% because here, a rouleau is defined as a singlet or a doublet or a multiplet. It is clear that each patient holds a

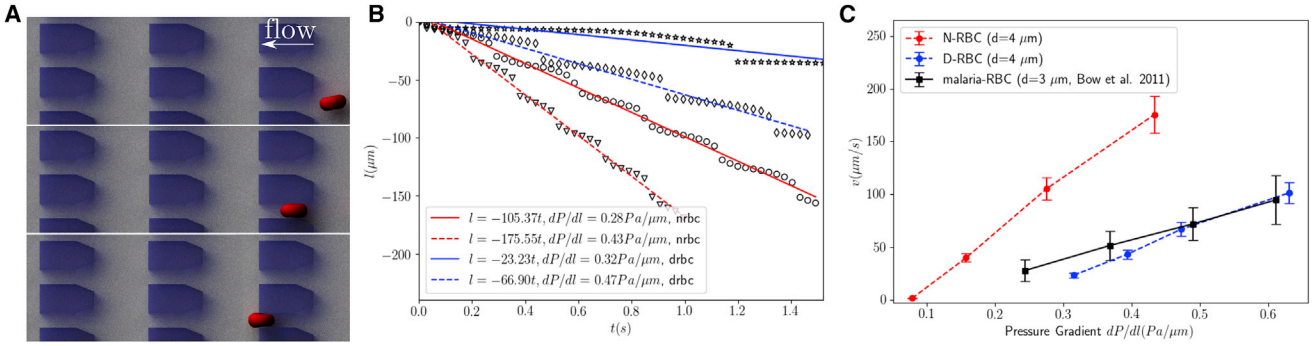

FIGURE 6 Simulation of single RBC dynamics driven by pressure gradient in the microfluidic device. (*A*) An example of a single D-RBC passing through microgates. Time-dependent trajectories (distance traveled *l*) of a single (*B*) N-RBC and (*C*) D-RBC along the flow direction under different pressure gradients. (*D*) Functional dependence of a single N-RBC (*red dashed line*) and a D-RBC (*black solid line*) velocity with respect to pressure gradient with comparison to similar experimental results by Bow et al. (60) on malaria-infected RBC, which is typically stiffer than N-RBC, in a microfluidic device similar to ours. *d* denotes the size of the gap between neighboring microgates, which RBCs can travel through. Both types of RBC require a nonzero pressure gradient for the onset of squeezing through microgates. However, to maintain a similar traveling speed, D-RBCs typically require a large pressure gradient than N-RBCs, given the horizontal gap between the curves mainly due to the larger shear modulus and oblate shape of D-RBCs, which is also implied by the difference in the slope of the curves. To see this figure in color, go online.

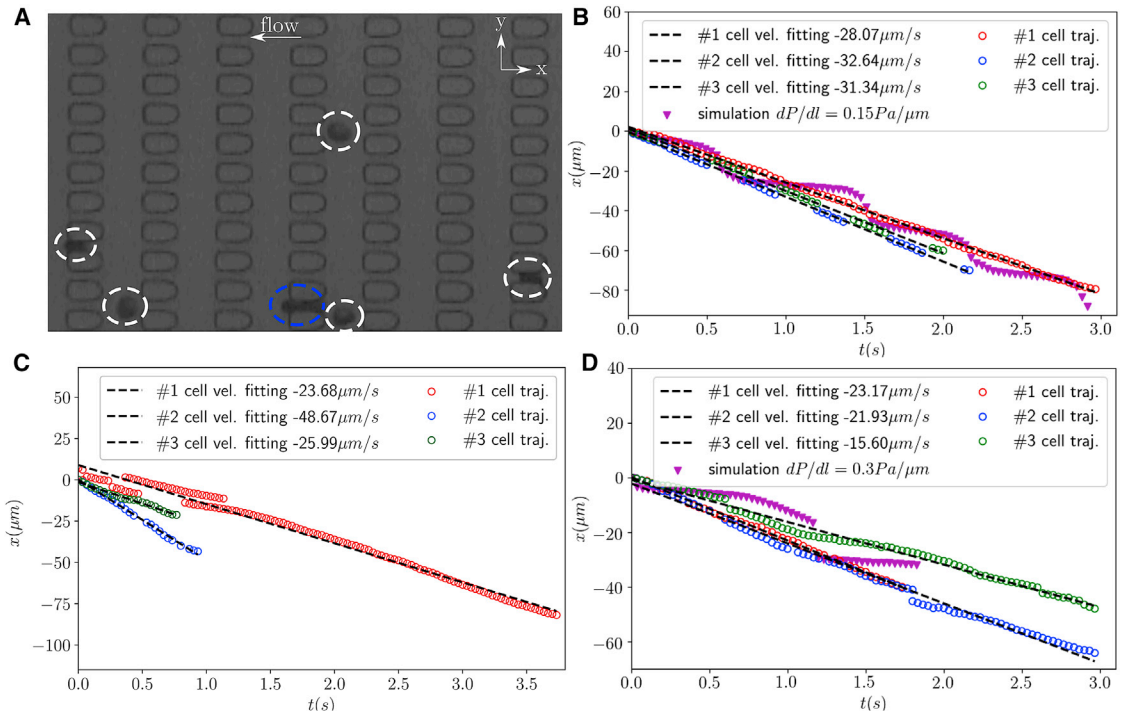

FIGURE 7 Overview for monitoring single RBC motion in the microfluidic device. (*A*) A typical snapshot, which is a zoomed-in figure of the ROI, selected from in vitro experiments with single RBCs (in the white *dashed circles*) near a doublet (in the *blue dashed circle*). Trajectories of three neighboring single RBCs in the microfluidic experiments are shown for (*B*) patient II (obese without T2DM) with validation of pressure gradient at $dP/dl = 0.15$ Pa/μm, (*C*) patient IV (well-controlled T2DM), and (*D*) patient V (poorly controlled T2DM) with validation of pressure gradient $dP/dl = 0.3$ Pa/μm and corresponding single-cell trajectory (*magenta triangles*) in simulation. Magenta triangles in (*B*) and (*D*) represent the simulated cell trajectories under given pressure gradient. Red, green, and blue circles represent cell trajectories at each instant measured in microfluidic experiments, and black dashed lines represent a linear fitting of corresponding trajectories, see figure legends for the fitted velocity; the minus signs in the velocities imply that RBC travels along the $-x$ direction. To see this figure in color, go online.

share of three types of rouleau, i.e., every patient has singlets, doublets, and multiplets, despite their lab test showing distinct fibrinogen concentration levels. In addition, from the three selected patient samples, we also note that the percentage of rouleaux of different lengths varies from patient to patient and is positively correlated with their fibrinogen concentration levels. Informed by these observations, we construct patient-specific RBC models from the three groups shown in Fig. 2 *D*, i.e., the weak, medium, and strong groups, and assume that for each patient, the percentage of weak, medium, and strong adhesive dynamics is determined by their own rouleau length distributions. Although heterogeneous distribution of RBC-RBC adhesion is expected, to the best of our knowledge, there are currently no direct experimental data available about the distribution of cell-cell adhesion for RBC. Hence, our model setup here is based on the direct observations from our microfluidic experiments that the rouleau length distribution is seemingly correlated to the adhesion strength among rouleaux. To demonstrate the overall cell-cell adhesive interaction for each patient, we plot the averaged "interactive vertices ratio" of patient-specific RBC models implemented in simulations; see Fig. 8 *B*.

To validate the experiment-informed RBC model, we compare patient-specific rouleau dissociation rates at doublet level. In the experiment, we keep track of 20 doublets and record the number of doublets that are fully separated before they exit the ROI (see the *unshaded bars* in Fig. 8 *C*). On the other hand, for each patient we simulate 25 patient-specific doublets passing through microgates and calculate the percentage of fully separated doublets over the total amount of doublets observed (see the *shaded bars* in Fig. 8 *C*). The simulation and experimental results agree well with each other, confirming that the distribution of rouleau length is an important indicator in doublet breakup dynamics. Additionally, our simulation results show that under the same pressure gradient, T2DM doublets with weak cell-cell adhesion strength easily break up, becoming singlets (see Video S7), whereas doublets with medium cell-cell adhesion strength mostly maintain the rouleau length (see Video S8), and doublets with strong cell-cell adhesion strength are robust enough to maintain the adhered state and hence have higher probabilities to become a longer rouleau later (see Video S9). These observations, consistent with experimental records, validate our patient-specific RBC model construction. Additionally,

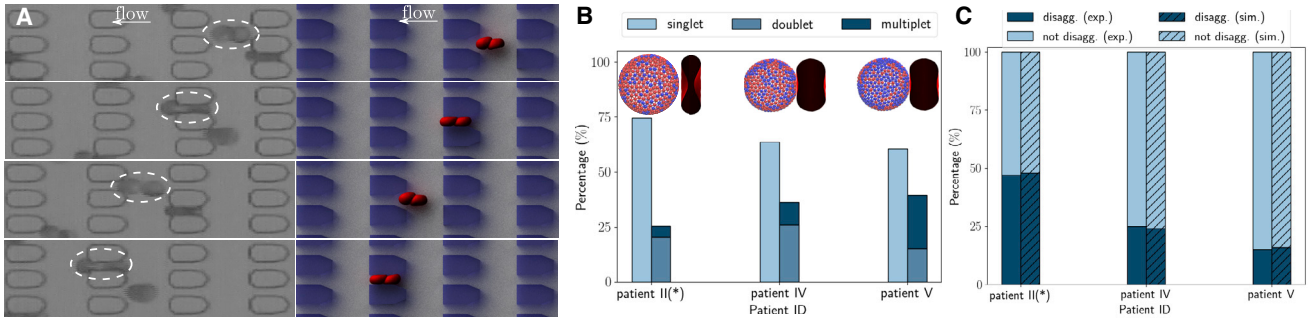

FIGURE 8 Statistical quantification of the aggregation strength through in vitro experiments and simulations for selective patients. (*A*) An example of a T2DM doublet (in the *white dashed circles*) with strong cell-cell aggregation passing through microgates in experiment (*left column*) and simulation (*right column*) without the occurrence of doublet breakup event before it exits the ROI. (*B*) Patient-specific experimental results on the percentage of rouleaux with different lengths, i.e., the count of singlets, doublets, and multiplets divided by the total count of rouleaux, respectively. On top of each patient's rouleau length distribution, we draw a representative RBC to reflect the averaged interactive vertices coverage of those simulated RBCs for that patient. (*C*) Comparison between experimental and simulated patient-specific doublet dissociation rate; exp. is short for experiment and sim. for simulation. To see this figure in color, go online.

this demonstrates that with increasing disease severity, indicated by higher HbA1c and higher fibrinogen levels, our patient-specific RBC models predict the increased formation of multiplets and decreased dissociation rates of doublets.

From our microfluidic experiments, we notice that the alignment of a long rouleau with respect to the flow direction plays a key role in its breakup pattern afterwards. To probe this phenomenon qualitatively, we carry out simulations on two 10-cell rouleaux (representing a long rouleau) passing through the microgates (see Fig. 9 *A* and Video S10 for a rouleau entering the microchannel along the flow direction; see also Fig. 9 *B* and Video S11 for another rouleau entering microchannel with a 21° angle to the flow direction). Note that this type of extremely long rouleau is frequently seen in the sample of T2DM patients like patient V; therefore, we adopt the D-RBC model with 100% interactive vertices ratio in Fig. 2 *D*. Additionally, to provide enough statistics, we run each simulation set for five times and obtain the rouleau length distribution at the outlet of the microchannel (see the *last row* in Fig. 9). The snapshots show that these two rouleaux experience distinct collisions with the microgates and hence exhibit different breakup patterns. The rouleau with an inclined centerline breaks up into several triplets and one quadruplet, whereas the rouleau having its centerline parallel to flow direction splits into two doublets and two triplets. This suggests that the inclination angle between rouleau centerline and flow direction can significantly affect the corresponding rouleau breakup patterns. Other studies in the literature also showed similar observations. For example, Ji et al. (65) applied microfilters to separate white blood cells (WBCs) from RBCs within plasma and suggested that RBC aggregation will lead to filter clogging. They also compared the RBC separation and WBC trapping efficiency of microfluidic devices with a

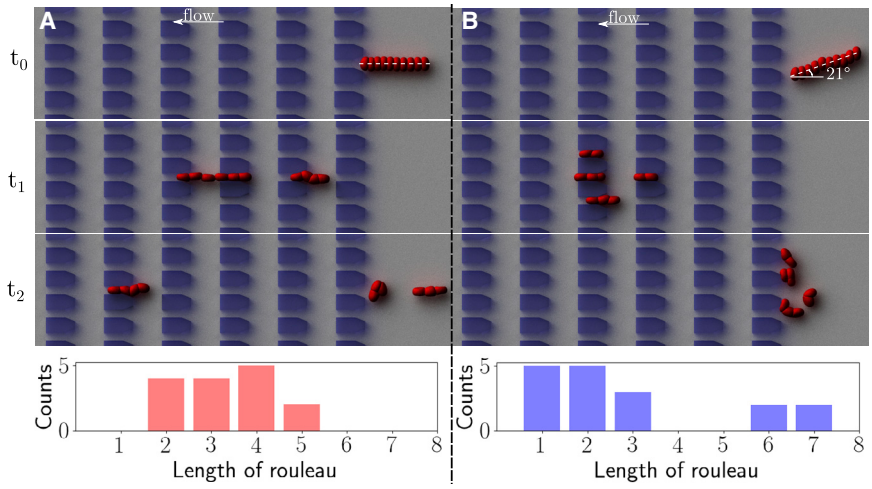

FIGURE 9 Different breakup patterns of two 10-cell rouleaux when passing through microgates under the same pressure gradient at $\Delta P/\Delta l = 0.4$ Pa/μm, where the centerline of RBCs in one rouleau is (*A*) parallel to and another has (*B*) a 21° inclination angle to the direction of flow ($t_0 = 0$ s, $t_1 \approx 3$ s, $t_2 \approx 4.5$ s). With successive collisions with the microgates, these 10-cell rouleaux eventually break up into rouleaux of shorter lengths. The corresponding outlet rouleau length distribution is shown in the last row. In (*A*), the 10-cell rouleau tends to break up into rouleaux of evenly distributed lengths, suggested by the concentrated counts around three-cell and four-cell rouleaux, whereas in (*B*), the 10-cell rouleau breaks up to rouleaux of very different lengths. For each case, five different simulation tests are performed to record the lengths of shorter rouleaux produced by the rupture of 10-cell rouleau. Video clip for (*A*) is provided in Video S10 and for (*B*) in Video S11. To see this figure in color, go online.

weir filter, a pillar filter, and crossflow filters with slits slanted 60° and 90°, respectively. They concluded that the crossflow design could be the filter of choice because of its convenience in fabrication and high efficiency in cell sorting (65). We note that the slanted slits of the microfilter in their work is equivalent to the inclination angle between the centerline of rouleau and flow direction in our simulations. Therefore, our simulation of rouleau breakups at multiplet level could guide the design of microfluidic device and improve the efficiency of separating aggregatable cells.

CONCLUSION

RBCs in patients with T2DM are associated with reduced cell deformability and elevated cell aggregation, both of which make whole blood more viscous compared with healthy individuals, leading to impaired microcirculation. From the clinical point of view, it is recognized that Hb1Ac level is positively associated with microvascular complications in T2DM (66–68). Some studies have also shown that fibrinogen level is also positively correlated with microvascular complications (69,70). In this work, to enhance our understanding of fibrinogen-dependent RBC aggregation, which contributes to the abnormal microvascular complications in T2DM, we conducted microfluidic experiments with blood samples from six obese patients with and without T2DM and extracted informative statistics to develop patient-specific RBC models. We performed experiment-informed simulations on the patient-specific cell-cell detachment process of rouleaux at the doublet and multiplet levels and validated the patient-specific RBC models by comparing the simulation results with data from experiments. We note here that although we simulate the RBC dynamics of two T2DM patients (patient IV and patient V) who are on different medications and represent well-controlled and poorly controlled patients, respectively, our results for these two patients do not imply in one way or the other the effectiveness of the medications (see Table S1 for details of medications).

To construct fibrinogen-dependent RBC adhesion models, we determined the model parameters through quantitatively matching the rouleau breakup forces obtained from simulations mimicking AFM and OT tests to the corresponding experimental data. Further validation of the fibrinogen-dependent RBC models was conducted by comparing the patient-specific simulation results with our in vitro microfluidic experiments on three selected patients (II, IV, and V, representing obesity without T2D and obesity with good and with bad control of T2DM, respectively). With increasing disease severity, indicated by higher HbA1c and higher fibrinogen levels in patients' blood, our patient-specific RBC model predicts the increased formation of multiplets and decreased dissociation rates of doublets. The simulations of the microfluidic experiments match the observed patient-specific doublet breakup rates, as well as the long rouleau breakup patterns. The simulation results show that given the same pressure gradient, the T2DM doublets with weak cell-cell adhesive interaction tend to break up easily, the T2DM doublets with medium cell-cell adhesive interaction strength mostly maintain the rouleau structure, and those with strong cell-cell adhesive interaction strength are extremely robust.

In addition, for poorly controlled T2DM patients, we notice the frequent existence of extremely long rouleaux in their blood samples, which is rarely seen in an obese patient without T2DM, whose plasma fibrinogen concentration level is relatively lower than that from patients with T2DM. By observing the dynamics of these extremely long rouleaux in the microfluidic device, we found that the alignment of rouleaux with respect to flow direction can affect their breakup patterns after repetitive collisions with the walls of microgates. We confirmed the observed characteristics through simulations of angle-dependent rouleau breakup dynamics at the multiplet level. The angle-dependent rouleau breakup patterns captured by our simulations may help improve the design of microfluidic devices that are used to perform cell sorting or cell separation, especially those involving cell-cell adhesion. More importantly, it justifies further research in patients with T2DM, who, because of plaque formation and thus capillary lumen irregularities, may demonstrate higher exposure to angled rouleau-wall collisions. Hence, our microfluidic experiments, patient-specific cell-cell interaction RBC models, and experiment-informed simulations seamlessly incorporate information from patient blood samples, fluid dynamics inside the microchannel, and associated hemodynamics, providing a, to our knowledge, novel way to quantify the heterogeneous patient-specific rouleau dynamics in a capillary-like microenvironment.

SUPPORTING MATERIAL

Supporting Material can be found online at https://doi.org/10.1016/j.bpj.2020.07.026.

AUTHOR CONTRIBUTIONS

Y.D., D.P.P., X.L., N.P., C.S.M., M.D., and G.E.K. designed research. Y.D. carried out all the simulations. D.P.P. performed the microfluidic experiments. N.P. and C.S.M. collected the clinical information and samples, provided the blood samples for the study, and performed biochemical measurements. X.L., M.D., C.S.M., and G.E.K. contributed new reagents and analysis tools. Y.D., D.P.P., X.L., M.D., and G.E.K. analyzed data. All authors contributed to writing the manuscript.

ACKNOWLEDGMENTS

We acknowledge the support from U01HL142518. C.S.M. acknowledges the support from National Institutes of Health K24DK081913 for the clinical part and biochemical measurements. N.P. was funded by the Deutsche Forschungsgemeinschaft (German Research Foundation)-389891681 (PE

2431/2-1). Computations were supported by the National Science Foundation XSEDE resources award No. TG-DMS140007 and No. TCMBC190045.

REFERENCES

1. Chatterjee, S., K. Khunti, and M. J. Davies. 2017. Type 2 diabetes. *Lancet.* 389:2239–2251.
2. Cho, H. C. 2011. The relationship among homocysteine, bilirubin, and diabetic retinopathy. *Diabetes Metab. J.* 35:595–601.
3. Brazionis, L., K. Rowley, Sr., …, K. O'Dea. 2008. Homocysteine and diabetic retinopathy. *Diabetes Care.* 31:50–56.
4. Young, M. J., A. J. Boulton, …, P. H. Sonksen. 1993. A multicentre study of the prevalence of diabetic peripheral neuropathy in the United Kingdom hospital clinic population. *Diabetologia.* 36:150–154.
5. Davies, M., S. Brophy, …, A. Taylor. 2006. The prevalence, severity, and impact of painful diabetic peripheral neuropathy in type 2 diabetes. *Diabetes Care.* 29:1518–1522.
6. Jeganathan, V. S. E., J. J. Wang, and T. Y. Wong. 2008. Ocular associations of diabetes other than diabetic retinopathy. *Diabetes Care.* 31:1905–1912.
7. Mather, K. J., S. Verma, and T. J. Anderson. 2001. Improved endothelial function with metformin in type 2 diabetes mellitus. *J. Am. Coll. Cardiol.* 37:1344–1350.
8. Vinik, A. I., T. Erbas, …, G. L. Pittenger. 2001. Platelet dysfunction in type 2 diabetes. *Diabetes Care.* 24:1476–1485.
9. Spectre, G., C.-G. Östenson, …, P. Hjemdahl. 2012. Postprandial platelet activation is related to postprandial plasma insulin rather than glucose in patients with type 2 diabetes. *Diabetes.* 61:2380–2384.
10. Vallés, J., M. T. Santos, …, R. Carmena. 1997. Modulatory effect of erythrocytes on the platelet reactivity to collagen in IDDM patients. *Diabetes.* 46:1047–1053.
11. Schmid-Schönbein, H., and E. Volger. 1976. Red-cell aggregation and red-cell deformability in diabetes. *Diabetes.* 25:897–902.
12. McMillan, D. E. 1983. The effect of diabetes on blood flow properties. *Diabetes.* 32:56–63.
13. Fedosov, D. A., W. Pan, …, G. E. Karniadakis. 2011. Predicting human blood viscosity in silico. *Proc. Natl. Acad. Sci. USA.* 108:11772–11777.
14. Wysocki, M., M. Krotkiewski, …, U. Bagge. 1991. Hemorheological disturbances, metabolic parameters and blood pressure in different types of obesity. *Atherosclerosis.* 88:21–28.
15. Brun, J.-F., I. Aloulou, and E. Varlet-Marie. 2004. Hemorheological aspects of the metabolic syndrome: markers of insulin resistance, obesity or hyperinsulinemia? *Clin. Hemorheol. Microcirc.* 30:203–209.
16. Wiewiora, M., J. Piecuch, …, K. Sosada. 2015. The effects of weight loss surgery on blood rheology in severely obese patients. *Surg. Obes. Relat. Dis.* 11:1307–1314.
17. Cloutier, G., A. Zimmer, …, J.-L. Chiasson. 2008. Increased shear rate resistance and fastest kinetics of erythrocyte aggregation in diabetes measured with ultrasound. *Diabetes Care.* 31:1400–1402.
18. Beamer, N., G. Giraud, …, B. Coull. 1997. Diabetes, hypertension and erythrocyte aggregation in acute stroke. *Cerebrovasc. Dis.* 7:144–149.
19. Cho, Y. I., M. P. Mooney, and D. J. Cho. 2008. Hemorheological disorders in diabetes mellitus. *J. Diabetes Sci. Technol.* 2:1130–1138.
20. Le Devehat, C., M. Vimeux, …, A. Bertrand. 1989. Red blood cell aggregation and disaggregation in diabetes mellitus. *Clin. Hemorheol. Microcirc.* 9:845–854.
21. Waitzman, M. B., A. M. Colley, and K. Nardelli-Olkowska. 1977. Metabolic approaches to studies on diabetic microangiopathy. *Diabetes.* 26:510–517.
22. Krüger-Genge, A., R. Sternitzky, …, F. Jung. 2019. Erythrocyte aggregation in relation to plasma proteins and lipids. *J. Cell. Biotechnol.* 5:65–70.
23. Chien, S., L. A. Sung, …, S. Usami. 1977. Determination of aggregation force in rouleaux by fluid mechanical technique. *Microvasc. Res.* 13:327–333.
24. Brust, M., O. Aouane, …, C. Wagner. 2014. The plasma protein fibrinogen stabilizes clusters of red blood cells in microcapillary flows. *Sci. Rep.* 4:4348.
25. Flormann, D., O. Aouane, …, C. Wagner. 2017. The buckling instability of aggregating red blood cells. *Sci. Rep.* 7:7928.
26. Neu, B., and H. J. Meiselman. 2002. Depletion-mediated red blood cell aggregation in polymer solutions. *Biophys. J.* 83:2482–2490.
27. Shin, S., J.-H. Nam, …, J.-S. Suh. 2009. A transient, microfluidic approach to the investigation of erythrocyte aggregation: the threshold shear-stress for erythrocyte disaggregation. *Clin. Hemorheol. Microcirc.* 42:117–125.
28. Lee, B.-K., J. Y. Ko, …, S. Shin. 2012. Investigation of critical shear stress with simultaneous measurement of electrical impedance, capacitance and light backscattering. *Clin. Hemorheol. Microcirc.* 51:203–212.
29. Samocha-Bonet, D., R. Ben-Ami, …, S. Berliner. 2004. Flow-resistant red blood cell aggregation in morbid obesity. *Int. J. Obes. Relat. Metab. Disord.* 28:1528–1534.
30. Bronkhorst, P. J., J. Grimbergen, …, J. J. Sixma. 1997. The mechanism of red cell (dis)aggregation investigated by means of direct cell manipulation using multiple optical trapping. *Br. J. Haematol.* 96:256–258.
31. Lee, K., M. Kinnunen, …, A. A. Fedyanin. 2016. Optical tweezers study of red blood cell aggregation and disaggregation in plasma and protein solutions. *J. Biomed. Opt.* 21:35001.
32. Ashkin, A. 1970. Acceleration and trapping of particles by radiation pressure. *Phys. Rev. Lett.* 24:156.
33. Avsievich, T., A. Popov, …, I. Meglinski. 2018. Mutual interaction of red blood cells assessed by optical tweezers and scanning electron microscopy imaging. *Opt. Lett.* 43:3921–3924.
34. Steffen, P., C. Verdier, and C. Wagner. 2013. Quantification of depletion-induced adhesion of red blood cells. *Phys. Rev. Lett.* 110:018102.
35. Guedes, A. F., F. A. Carvalho, …, N. C. Santos. 2017. Essential arterial hypertension patients present higher cell adhesion forces, contributing to fibrinogen-dependent cardiovascular risk. *Nanoscale.* 9:14897–14906.
36. Guedes, A. F., C. Moreira, …, F. A. Carvalho. 2019. Fibrinogen-erythrocyte binding and hemorheology measurements in the assessment of essential arterial hypertension patients. *Nanoscale.* 11:2757–2766.
37. Xiao, L., Y. Liu, …, B. Fu. 2016. Simulation of deformation and aggregation of two red blood cells in a stenosed microvessel by dissipative particle dynamics. *Cell Biochem. Biophys.* 74:513–525.
38. Xiao, L., C. Lin, …, W. Yan. 2020. Effects of red blood cell aggregation on the blood flow in a symmetrical stenosed microvessel. *Biomech. Model. Mechanobiol.* 19:159–171.
39. Ye, T., N. Phan-Thien, …, C. T. Lim. 2014. Dissipative particle dynamics simulations of deformation and aggregation of healthy and diseased red blood cells in a tube flow. *Phys. Fluids.* 26:111902.
40. Ye, T., and L. Peng. 2019. Motion, deformation, and aggregation of multiple red blood cells in three-dimensional microvessel bifurcations. *Phys. Fluids.* 31:021903.
41. Fenech, M., D. Garcia, …, G. Cloutier. 2009. A particle dynamic model of red blood cell aggregation kinetics. *Ann. Biomed. Eng.* 37:2299–2309.
42. Xu, D., E. Kaliviotis, …, J. Williams. 2013. Large scale simulation of red blood cell aggregation in shear flows. *J. Biomech.* 46:1810–1817.
43. Hoore, M., F. Yaya, …, D. A. Fedosov. 2018. Effect of spectrin network elasticity on the shapes of erythrocyte doublets. *Soft Matter.* 14:6278–6289.
44. Du, E., M. Diez-Silva, …, S. Suresh. 2015. Kinetics of sickle cell biorheology and implications for painful vasoocclusive crisis. *Proc. Natl. Acad. Sci. USA.* 112:1422–1427.

45. Li, X., E. Du, …, G. E. Karniadakis. 2017. Patient-specific modeling of individual sickle cell behavior under transient hypoxia. *PLoS Comput. Biol.* 13:e1005426.

46. Papageorgiou, D. P., S. Z. Abidi, …, M. Dao. 2018. Simultaneous polymerization and adhesion under hypoxia in sickle cell disease. *Proc. Natl. Acad. Sci. USA.* 115:9473–9478.

47. Chang, H.-Y., X. Li, and G. E. Karniadakis. 2017. Modeling of biomechanics and biorheology of red blood cells in type 2 diabetes mellitus. *Biophys. J.* 113:481–490.

48. Chang, H.-Y., A. Yazdani, …, G. E. Karniadakis. 2018. Quantifying platelet margination in diabetic blood flow. *Biophys. J.* 115:1371–1382.

49. Lowe, G., M. Woodward, …, J. Chalmers. 2014. Circulating inflammatory markers and the risk of vascular complications and mortality in people with type 2 diabetes and cardiovascular disease or risk factors: the ADVANCE study. *Diabetes.* 63:1115–1123.

50. Pivkin, I. V., and G. E. Karniadakis. 2008. Accurate coarse-grained modeling of red blood cells. *Phys. Rev. Lett.* 101:118105.

51. Fedosov, D. A., H. Lei, …, G. E. Karniadakis. 2011. Multiscale modeling of red blood cell mechanics and blood flow in malaria. *PLoS Comput. Biol.* 7:e1002270.

52. Peng, Z., X. Li, …, S. Suresh. 2013. Lipid bilayer and cytoskeletal interactions in a red blood cell. *Proc. Natl. Acad. Sci. USA.* 110:13356–13361.

53. Fedosov, D. A., B. Caswell, …, G. E. Karniadakis. 2011. Quantifying the biophysical characteristics of Plasmodium-falciparum-parasitized red blood cells in microcirculation. *Proc. Natl. Acad. Sci. USA.* 108:35–39.

54. Lei, H., and G. E. Karniadakis. 2013. Probing vasoocclusion phenomena in sickle cell anemia via mesoscopic simulations. *Proc. Natl. Acad. Sci. USA.* 110:11326–11330.

55. Li, H., L. Lu, …, S. Suresh. 2018. Mechanics of diseased red blood cells in human spleen and consequences for hereditary blood disorders. *Proc. Natl. Acad. Sci. USA.* 115:9574–9579.

56. Deng, Y., D. P. Papageorgiou, …, G. E. Karniadakis. 2019. Quantifying shear-induced deformation and detachment of individual adherent sickle red blood cells. *Biophys. J.* 116:360–371.

57. Vague, P., and I. Juhan. 1983. Red cell deformability, platelet aggregation, and insulin action. *Diabetes.* 32:88–91.

58. Bäumler, H., B. Neu, …, H. Kiesewetter. 1999. Basic phenomena of red blood cell rouleaux formation. *Biorheology.* 36:439–442.

59. Pivkin, I. V., and G. E. Karniadakis. 2006. Controlling density fluctuations in wall-bounded dissipative particle dynamics systems. *Phys. Rev. Lett.* 96:206001.

60. Bow, H., I. V. Pivkin, …, J. Han. 2011. A microfabricated deformability-based flow cytometer with application to malaria. *Lab Chip.* 11:1065–1073.

61. Zhang, Y., C. Huang, …, S. Suresh. 2015. Multiple stiffening effects of nanoscale knobs on human red blood cells infected with Plasmodium falciparum malaria parasite. *Proc. Natl. Acad. Sci. USA.* 112:6068–6073.

62. Hosseini, S. M., and J. J. Feng. 2012. How malaria parasites reduce the deformability of infected red blood cells. *Biophys. J.* 103:1–10.

63. Agrawal, R., T. Smart, …, C. Pavesio. 2016. Assessment of red blood cell deformability in type 2 diabetes mellitus and diabetic retinopathy by dual optical tweezers stretching technique. *Sci. Rep.* 6:15873.

64. Tsukada, K., E. Sekizuka, …, H. Minamitani. 2001. Direct measurement of erythrocyte deformability in diabetes mellitus with a transparent microchannel capillary model and high-speed video camera system. *Microvasc. Res.* 61:231–239.

65. Ji, H. M., V. Samper, …, L. Yobas. 2008. Silicon-based microfilters for whole blood cell separation. *Biomed. Microdevices.* 10:251–257.

66. Bennett, C. M., M. Guo, and S. C. Dharmage. 2007. HbA(1c) as a screening tool for detection of Type 2 diabetes: a systematic review. *Diabet. Med.* 24:333–343.

67. Sartore, G., N. C. Chilelli, …, A. Lapolla. 2013. Association between glucose variability as assessed by continuous glucose monitoring (CGM) and diabetic retinopathy in type 1 and type 2 diabetes. *Acta Diabetol.* 50:437–442.

68. Penno, G., A. Solini, …, G. Pugliese; Renal Insufficiency And Cardiovascular Events Study Group. 2013. HbA1c variability as an independent correlate of nephropathy, but not retinopathy, in patients with type 2 diabetes: the Renal Insufficiency and Cardiovascular Events (RIACE) Italian multicenter study. *Diabetes Care.* 36:2301–2310.

69. Le, D. S. N., R. Miles, …, J. Krakoff. 2008. The association of plasma fibrinogen concentration with diabetic microvascular complications in young adults with early-onset of type 2 diabetes. *Diabetes Res. Clin. Pract.* 82:317–323.

70. Ernst, E. 1990. Plasma fibrinogen–an independent cardiovascular risk factor. *J. Intern. Med.* 227:365–372.

71. Lominadze, D., and W. L. Dean. 2002. Involvement of fibrinogen specific binding in erythrocyte aggregation. *FEBS Lett.* 517:41–44.

Biophysical Journal, Volume *119*

Supplemental Information

Quantifying Fibrinogen-Dependent Aggregation of Red Blood Cells in Type 2 Diabetes Mellitus

Yixiang Deng, Dimitrios P. Papageorgiou, Xuejin Li, Nikolaos Perakakis, Christos S. Mantzoros, Ming Dao, and George Em Karniadakis

Supporting Materials:

Quantifying Fibrinogen-dependent Aggregation of Red Blood Cells in Type 2 Diabetes Mellitus

Yixiang Deng, Dimitrios P. Papageorgiou, Xuejin Li, Nikolaos Perakakis, Christos S. Mantzoros, Ming Dao, George Em Karniadakis

Summary of patient metabolism indices and medication history

To substantiate our claims in this work, we measure and summarize the metabolism indices and medication history of patients in Tab. S1. In particular, we confirm that patients are all obese, indicated from their BMIs (BMI≥25). More importantly, the selected patient II, IV and V for simulations are representatives from healthy, well-controlled T2DM and poorly-controlled T2DM patients, respectively, indicated by their Hb1Ac levels in Tab. 1 in the main text.

TABLE S1: **Measurement of Patients' Metabolistic Characteristics.**[1]

Patient ID	I	II	III	IV	V	VI
Age (y)	57	65	64	46	60	61
Weight (kg)	127.1	99.8	103.3	137.8	116.9	105.4
Height (cm)	170.7	170.5	176.2	166.3	192.9	179.1
BMI (kg/m^2)	43.62	34.33	33.27	49.83	31.42	32.86
Medications	No	No	Aspirin, Statin, HCT	Metformin	Metformin, ACE-inhibitor	Aspirin, Amlodipin, ACE-inhibitor, Statin
Glucose (mg/dl)	105	82	105	94	141	109
BUN (mg/dl)	9	10	18	13	11	9
Creatinine, Serum (mg/dl)	0.64	1.03	0.75	0.7	0.91	0.92
Sodium, Serum (mmol/l)	137	142	142	139	142	136
Potassium, Serum (mmol/l)	4.1	5.8	4.2	4.4	4.6	3.9
Chloride, Serum (mmol/l)	96	105	103	100	102	101
Carbon Dioxide, Total (mmol/L)	26	22	23	25	25	23

RBC models

We construct the following potential to represent the elastic energy of the RBC models,

$$V_s = \sum_{j\in 1,\dots,N_s} \left[\frac{k_B T l_m (3x_j^2 - 2x_j^3)}{4p(1-x_j)} + \frac{k_p}{(n-1)l_j^{n-1}} \right], \tag{1}$$

[1] HCT, Hydrochlorothiazide; BUN, blood urea nitrogen.

where p denotes the persistence length, l_i denotes the length of ith spring, l_0 denotes equilibrium spring length, l_m denotes maximal spring extension and k_BT is the energy unit. The bending resistance of the RBC membrane is achieved using the following potential,

$$V_b = \sum_{\alpha,\beta \text{ pair}} k_b[1 - \cos(\theta_{\alpha\beta} - \theta_0)], \tag{2}$$

where k_b is constant denoting the bending modulus, $\theta_{\alpha\beta}$ is the instantaneous angle between two adjacent triangles sharing a common edge and θ_0 is the spontaneous angle. Additionally, to impose area and volume conservation of RBC models due to the area conservation of the lipid bilayer and the incompressibility of the cytoplasm, we apply the following combined potentials,

$$V_{a+v} = \sum_{j\in 1,\ldots,N_t} \frac{k_d(A_j - A_0)^2}{2A_0} + \frac{k_a(A - A_0^{\text{tot}})^2}{2A_0^{\text{tot}}} + \frac{k_v(V - V_0^{\text{tot}})^2}{2V_0^{\text{tot}}}, \tag{3}$$

where k_a and k_v are area and volume constraint constants, and A is the instantaneous area of RBC during simulations.

Simulation model parameters

In all simulations presented in the main text, the parameters were calibrated based on experimental results then kept consistent unless otherwise noted in the main text.

Cell-cell interaction potentials

Detailed parameter values of the Morse potential and the Lennard-Jones potential are listed in Tab. S2.

TABLE S2: Model parameters for Morse potential and LJ potential.

Parameter	Simulation	Physical
r_0	1.0	1 μm
β	1.5	1.5 (scaling factor for distance, dimensionless)
σ	0.3	0.3 μm
ϵ	0.4	3.392×10^{-25}J
r_{LJ}	0.25	0.25 μm

Cell-fluid and fluid-fluid interaction

Under the DPD framework, the force F between a pair of atoms, for example, atom i and atom j, at a distance $r = |r_{ij}|$ within cutoff distance r_c, is given as a sum of three terms as follows,

$$\begin{aligned} F &= (F^C + F^D + F^R)r_{ij} \\ F^C &= Aw(r) \\ F^D &= -\gamma w^2(r)(r_{ij} \cdot v_{ij}) \\ F^R &= \sigma w(r)\alpha(\Delta t)^{-1/2} \\ w(r) &= (1 - r/r_c)^m \end{aligned}$$

where F^C is a conservative force, F^D is a dissipative force, and F^R is a random force. r_{ij} is a unit vector in the direction $r_i - r_j$, v_{ij} is the vector difference in velocities of atom i and atom j, α is a Gaussian random number with zero mean and unit variance, dt is the timestep size; m is an exponential factor and by setting it to 1 our DPD framework reduces to the standard DPD framework. We applied the same set of DPD parameters for cell-fluid and fluid-fluid interactions, as listed in Tab. S3.

TABLE S3: Model parameters for cell-cell and cell-fluid interactions.

Parameter	Simulation
A	2.5
γ	10
σ	1.414
m	0.25

Supporting movies

S1. Blood sample of patient II in microfluidic device.

S2. Blood sample of patient V in microfluidic device.

S3. Healthy doublet breaks up in simulation mimicking AFM.

S4. Healthy doublet breaks up in simulation mimicking OT.

S5. T2DM doublet breaks up in simulation mimicking OT.

S6. T2DM doublet breaks up in simulation mimicking AFM.

S7. T2DM doublet with weak cell-cell adhesive interaction passing through microgates.

S8. T2DM doublet with medium cell-cell adhesive interaction passing through microgates.

S9. T2DM doublet with strong cell-cell adhesive interaction passing through microgates.

S10. 10-cell rouleau entering microchannel along the flow direction.

S11. 10-cell rouleau entering microchannel with a 21° angle to flow direction.